Volume 13
Number 38
14 October 2025
Pages 11875–12308

Journal of Materials Chemistry B

Materials for biology and medicine

rsc.li/materials-b

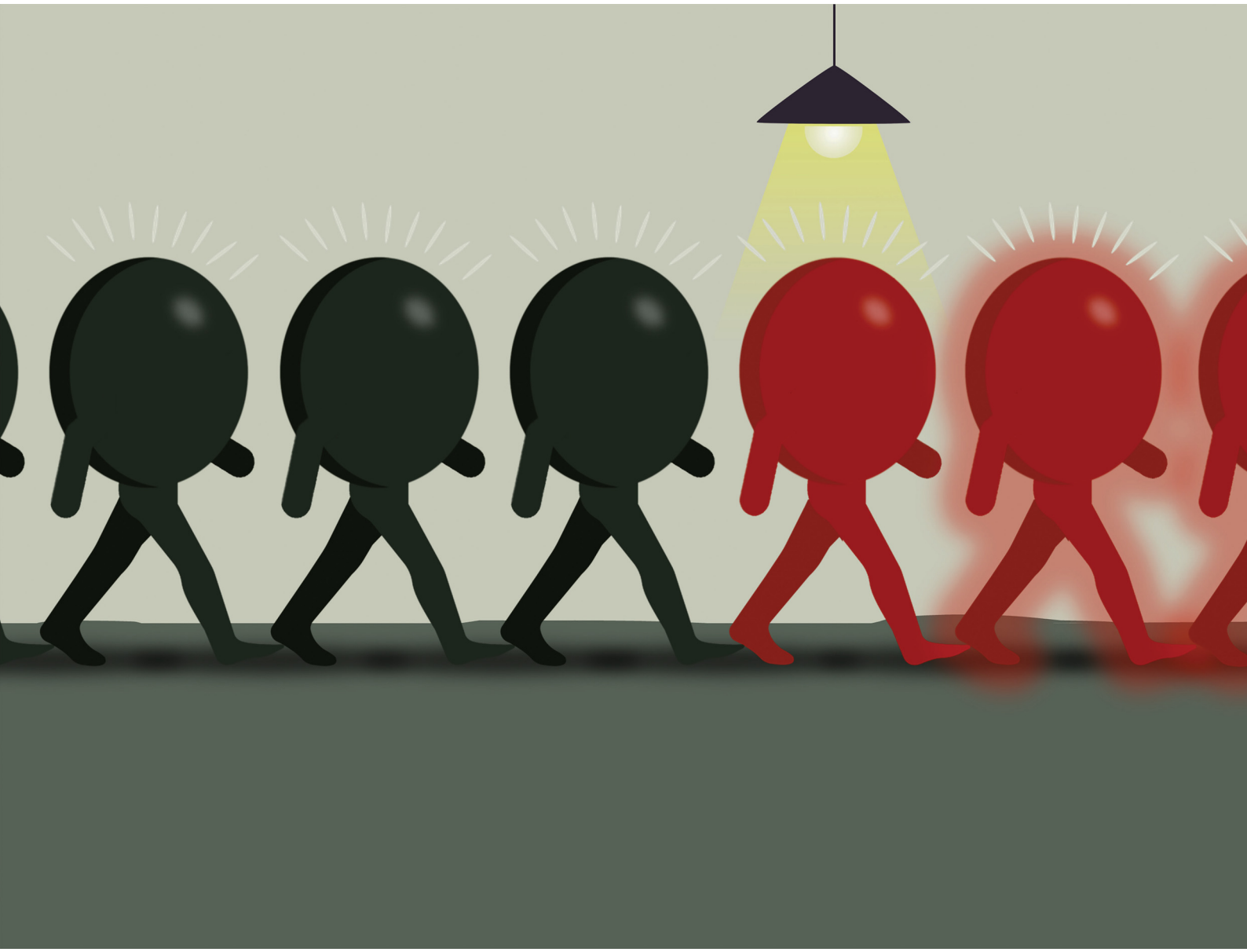

ISSN 2050-750X

ROYAL SOCIETY OF CHEMISTRY

PAPER

Raluca Borlan, Monica Focsan *et al.*
From fundamentals to applications: magnetic nanoparticles for MRI imaging and NIR-induced thermal activation in tissue-mimicking environments

Journal of Materials Chemistry B

ROYAL SOCIETY OF CHEMISTRY

PAPER

View Article Online
View Journal | View Issue

Cite this: J. Mater. Chem. B, 2025, 13, 12056

From fundamentals to applications: magnetic nanoparticles for MRI imaging and NIR-induced thermal activation in tissue-mimicking environments

Radu Lapusan,[a] Andreea Balmus,[ab] Radu Fechete,[cd] Bogdan Viorel Neamtu,[ef] Jessica Ponti,[g] Raluca Borlan *[b] and Monica Focsan *[ab]

Magnetic nanoparticles are widely explored in biomedical applications, particularly as MRI contrast agents and for magnetic hyperthermia. However, their photothermal capabilities under near-infrared (NIR) irradiation remain underexplored in realistic, tissue-like environments. This study provides a comprehensive assessment of ultrasmall Fe_3O_4 nanoparticles (9.23 ± 2.97 nm) in 3D agarose-based tissue-mimicking phantoms, integrating their imaging and photothermal properties under clinically relevant conditions. Photothermal performance was tested under 850, 970, and 1100 nm NIR light, with 970 nm showing optimal efficiency (71.59%) and a penetration depth of 2.1 cm. With a high saturation magnetization of approximately 52.4 emu g^{-1}, the nanoparticles were evaluated as MRI contrast nanoagents, showing notable T1–T2 contrast enhancement across various concentrations. Their performance was systematically compared with the commercial agent Gadovist through magnetic resonance relaxometry, high-field preclinical MRI at 11.7 T, and clinical MRI at 1.5 T, providing a comprehensive assessment across multiple imaging platforms and concentration ranges. While this study does not include biological *in vitro* or *in vivo* models, the use of phantoms replicating tissue optical and thermal properties, combined with clinical imaging systems and safety-compliant irradiation, creates a high-fidelity platform for translational evaluation. These results support the development of dual-mode theranostic platforms and lay the groundwork for future *in vivo* studies of MRI-guided photothermal cancer therapy.

Received 15th May 2025,
Accepted 21st August 2025

DOI: 10.1039/d5tb01160d

rsc.li/materials-b

1. Introduction

Magnetic nanoparticles have emerged as powerful tools in biomedical applications due to their magnetic responsiveness and ability to interact with external stimuli. Their capacity to respond to external magnetic fields and ease of functionalization makes them valuable targeting agents, utilizing both passive and active mechanisms. They are extensively studied in preclinical settings as contrast agents aiding magnetic resonance imaging (MRI), enabling tumor and lymph node characterization, and they also exhibit inherent therapeutic potential, *i.e.*, magnetic hyperthermia. Thus, magnetic nanoparticles represent a versatile platform in nanomedicine, enabling targeted drug delivery,[1] advanced imaging[2] and therapeutic interventions.[3]

In medical imaging, magnetic nanoparticles serve as contrast nanoagents, particularly in MRI, significantly enhancing spatial resolution and facilitating early disease detection. These agents improve spatial resolution by altering the local magnetic field, which enhances the contrast between different tissues and clearly delineates anatomical structures, allowing for more precise imaging. Compared to classical gadolinium (Gd)-based

[a] Biomolecular Physics Department, Faculty of Physics, Babes-Bolyai University, 1 M. Kogalniceanu Street, 400084, Cluj-Napoca, Romania. E-mail: radu.lapusan@ubbcluj.ro, andreea.balmus@ubbcluj.ro, monica.iosin@ubbcluj.ro
[b] Nanobiophotonics and Laser Microspectroscopy Centre, Interdisciplinary Research Institute on Bio-Nano-Sciences, Babes-Bolyai University, 42 T. Laurian Street, 400271, Cluj-Napoca, Romania. E-mail: raluca.borlan@ubbcluj.ro
[c] INSPIRE Platform, Interdisciplinary Research Institute on Bio-Nano-Sciences, Babes-Bolyai University, 11 A. Janos Street., 400028, Cluj-Napoca, Romania. E-mail: radu.fechete@ubbcluj.ro
[d] Physics and Chemistry Department, Faculty of Material and Environmental Engineering, Technical University of Cluj-Napoca, 103-105 Muncii Avenue, 400641, Cluj-Napoca, Romania
[e] Materials Science and Engineering Department, Technical University of Cluj-Napoca, 103–105 Muncii Avenue, 400641, Cluj-Napoca, Romania. E-mail: bogdan.neamtu@stm.utcluj.ro
[f] EUT+ Institute of Nanomaterials and Nanotechnologies-EUTINN, European University of Technology, European Union
[g] European Commission, Joint Research Centre (JRC), 2749 E. Fermi Street, 21027, Ispra, Italy. E-mail: jessica.ponti@ec.europa.eu

contrast agents, magnetic nanoparticles offer enhanced safety, targeted imaging capabilities, and reduced tissue accumulation, presenting significant clinical advantages. They are emerging as a promising alternative to traditional contrast agents due to their unique properties and advantages. Magnetic nanoparticles, such as iron oxide nanoparticles, are customizable and exhibit both longitudinal T_1 (spin–lattice) and transverse T_2 (spin–spin) relaxation time effects, allowing for enhanced imaging flexibility.[4] They offer reduced toxicity compared to traditional Gd-based agents and are less likely to accumulate in tissues, minimizing the risks associated with Gd deposition disease. Additionally, magnetic nanoparticles can be engineered for multimodal imaging, integrating MRI with other imaging modalities thereby improving diagnostic accuracy and expanding their clinical applications.[2] Recent reports have also emphasized their theranostic potential, particularly for combined MR imaging and photothermal therapy applications.[5,6]

For example, they have been developed as dual MRI/PET imaging probes through surface modifications with polymers and targeting ligands, enabling radiolabeling with isotopes such as ^{64}Cu and ^{89}Zr. Studies have demonstrated their application in imaging lymph node metastases, prostate cancer and glioblastomas, with preclinical models utilizing various coatings, including dextran and human serum albumin, to optimize stability and biodistribution for enhanced imaging contrast in both modalities.[7] Building on bimodal MRI/PET imaging, researchers have expanded the functionality of magnetic iron–oxide nanoparticles to trimodal and even quadrimodal imaging by integrating additional contrast mechanisms. This has been achieved by co-loading iron–oxide nanoparticles with high-Z elements such as gold or bismuth to enhance computed tomography (CT) contrast or conjugating fluorescent dyes like Cy5.5 or IRDye800 for near-infrared fluorescence (NIRF) imaging. Additionally, hybrid constructs, such as gold/silica nanoparticles with paramagnetic and fluorescent lipid coatings, have been synthesized for multimodal applications, demonstrating enhanced visualization of macrophage cells *in vitro via* MRI, CT, and fluorescence imaging, as well as improved liver imaging *in vivo*. Further advancements have explored the use of magnetic nanoparticles in non-traditional multi-modal imaging techniques, including magnetic particle imaging, magneto-motive ultrasound, and magneto-photoacoustic imaging, where the nanoparticles themselves serve as the primary imaging source. These multi-functional nanosystems not only provide high spatial resolution and sensitivity across multiple imaging platforms but also pave the way for precision diagnostics, early disease detection, and real-time tracking of biological processes.[8–10]

Beyond imaging, magnetic nanoparticles also possess inherent therapeutic potential. When exposed to an alternating magnetic field (AMF), they generate localized heat through a process known as magnetic hyperthermia.[11] The temperature increase from the synergy of magnetic nanoparticles and magnetic fields arises through multiple mechanisms. For NPs smaller than 128 nm, super paramagnetic properties dominate, leading to Néel or Brownian relaxation. Néel relaxation generates heat through rapid magnetic moment realignment within the NP's crystalline structure, while Brownian relaxation results from NP movement-induced friction as they align with the AMF.[11] Although magnetic hyperthermia has been tested in a clinical setting on several occasions,[12] achieving precise heat delivery using magnetic fields is challenging due to its broad tissue penetration and limited spatial focus in standard clinical setups.

A novel and less explored therapeutic strategy arises when these nanoparticles are exposed to near-infrared (NIR) light. Magnetic nanoparticles can efficiently absorb NIR radiation and convert it into localized heat. Using focused NIR light from lasers or LEDs, the irradiation spot can be precisely confined to a specific target area, enabling selective and targeted treatment. Since the NIR region falls within the body's ''optical biological window,'' where tissue absorption is minimal, this approach allows deeper tissue penetration and precise thermal ablation of desired tissues, offering a minimally invasive therapeutic strategy, namely photothermal therapy (PTT).[13]

PTT is a rapidly advancing, minimally invasive cancer treatment that leverages NIR light to irradiate nanomaterials, inducing heat generation to selectively kill tumor cells. Compared to traditional therapies, PTT offers several advantages – it is less affected by side effects, can be repeated, and enhances the efficacy of radiotherapy and chemotherapy while also overcoming drug resistance. While various nanomaterials have been explored for PTT, their clinical translation is often hindered by challenges such as limited excretion, poor degradation, and potential toxicity.[14] A more promising approach involves harnessing the intrinsic optical properties of magnetic nanoparticles derived from electronic transitions in magnetic iron oxides. These transitions produce spectral absorption within the NIR therapeutic window, making them suitable for photothermal applications and providing magnetic nanoparticles with an additional heating mechanism alongside magnetic hyperthermia.[15,16] The use of NIR lasers in thermal cancer therapies offers advantages over an AMF, as AMF requires high current and voltage and cannot focus on a specific region, while NIR lasers exploit the biological window, where tissues become partially transparent due to reduced absorption and scattering, enhancing therapeutic precision.[17,18]

Building upon the aforementioned advantages, we synthesized ultrasmall magnetic nanoparticles and investigated their photothermal properties both in solution and when embedded in tissue-mimicking phantoms under various NIR light sources (850, 970 and 1100 nm LED and 980 nm laser). Moreover, their T1 and T2 dual imaging capabilities were tested on 11.7 T preclinical and 1.5 T clinical MRI systems using agarose-based phantoms. By integrating imaging with a fundamental understanding of magnetic and optical properties, this study aims to advance the development of multifunctional nanomaterials with broad biomedical applications.

2. Materials and methods

2.1 Materials

Iron(II) chloride 98%, iron(III) chloride 97%, and hexadecyltrimethylammonium bromide (CTAB) 98% were purchased from

Sigma-Aldrich. Ammonium hydroxide 25% was purchased from Nordic. For phantom production, agarose and intralipid 20% emulsion were purchased from Sigma-Aldrich.

Ultrapure water for all aqueous solutions was sourced from the Milli-Q purification system by Millipore, Merck (Massachusetts, USA).

2.2 Synthesis of magnetic nanoparticles

Magnetic nanoparticles were synthesized using a modified co-precipitation method, schematically illustrated in Scheme 1. Iron(II) and iron(III) salts, in a 4 : 5 weight ratio, were mixed in a round-bottom flask with CTAB as a stabilizing agent to prevent uncontrolled seeding; during the whole synthesis the mixture was stirred at room temperature at 300 rpm. Precipitation of iron oxide nanoparticles was initiated by the gradual addition of ammonium hydroxide to achieve and maintain a basic pH environment. This was managed by dropwise addition using an automated syringe pump, NE-1000-Programmable Single Syringe Pump from New Era Pump Systems Inc. (New York, USA), at a controlled rate of 1 mL per minute, ensuring precise reaction conditions. The reaction progress was continuously monitored, with completion indicated by a distinct transition in solution color from dark orange to black, confirming the formation of Fe_3O_4 nanoparticles.

Purification involved repeated centrifugation at 3400*g* for 10 minutes, followed by redispersion of the pellet in ultrapure water to remove unreacted precursors and byproducts.

Yield calculation. After purification, the iron oxide nanoparticles were dried in an oven at 45 °C overnight to obtain a constant weight. The dried nanoparticles were weighed using a precision analytical balance. The yield of the nanoparticle synthesis was calculated using eqn (1):

$$\text{yield } (\%) = \frac{\text{mass of dried nanoparticles}}{\text{total initial mass of iron(II) and iron(III) salts}} \times 100 \quad (1)$$

This calculation was performed for four independent synthesis batches to ensure reproducibility of the results. The initial mass of iron(II) (Fe^{2+}) and iron(III) (Fe^{3+}) salts was determined based on the quantities used in the synthesis, adjusted for the 4 : 5 weight ratio.

2.3 Embedding magnetic nanoparticles in tissue phantoms

To create a tissue-mimicking environment, a mixture of ultrapure water and agarose, prepared at a mass-to-volume ratio of approximately 1 : 25, was continuously stirred at 400 rpm and heated to 90 °C in a water bath. Agarose was gradually added until fully dissolved. Once a clear solution was obtained, intralipid solution was introduced at a 1 : 1 ratio with water, using the stock solution concentration, and stirring was continued for several minutes to ensure uniform distribution. For phantoms incorporating magnetic nanoparticles, the same protocol was followed, with the key modification that ultrapure water was replaced by suspensions of magnetic nanoparticles. These suspensions were prepared to achieve different final concentrations of magnetic nanoparticles (0.1, 1.7, 3.5, 6.9, 13.8, and 27.6 μM) and used separately during the initial mixing step. This adjustment ensured an even distribution of nanoparticles within the matrix, preserving the structural integrity of the phantom.

Finally, the prepared solutions were cast into specific molds based on the intended application: 2 mL centrifuge tubes (Eppendorf Safe-Lock centrifuge tubes, 2 mL, standard model) for photothermal studies and approximately 3 mL in a 24-well plate (CytoOne, TC-treated, clear polystyrene, standard model) for MRI experiments. The phantoms were allowed to solidify at room temperature for one hour before further analysis.

2.4 Detailed characterization

TEM (JEOL JEM-2100, JEOL, Italy) was used at 120 kV in TEM mode to characterize the morphology and size distribution of the magnetic nanoparticles. Sample suspensions (stock diluted 1 : 100 in MilliQ water), 3 μL, were manually deposited on a 200 mesh Formvar (Agar Scientific, USA) carbon-coated copper grid, pretreated using glow discharge (Leica EM ACE600, 10 mA, 30 sec.), under demagnetization conditions (Bergeon demagnetiser – 240 V, TAAB, UK) and dried overnight in a desiccator before analysis. Size distribution was calculated for over 1600 nanoparticles with ImageJ software (NanoDefine ParticleSizer plugin).

The hydrodynamic size and zeta potential of the magnetic nanoparticles were determined using a Zetasizer NanoZS90 instrument from Malvern Panalytical Ltd. (UK) at a constant temperature of 25 °C. Measurements were conducted in triplicate, employing disposable square polystyrene cuvettes (DTS0012) for

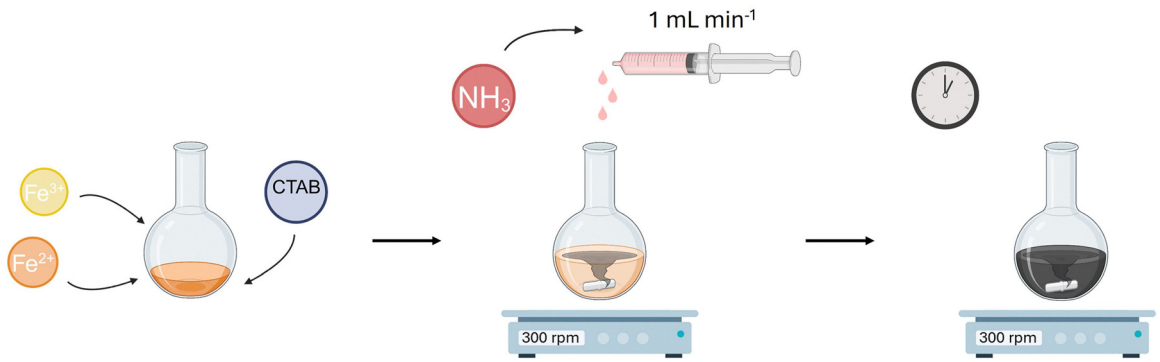

Scheme 1 Illustration of the synthesis method for magnetic nanoparticles. Created with BioRender.com.

dynamic light scattering (DLS) measurements and disposable folded capillary cells (DTS1070) for zeta-potential measurements.

The magnetic characteristics of the newly synthesized Fe_3O_4 nanoparticles were investigated *via* vibrating sample magnetometry (VSM) using a magnetometer produced by Nanomagnetic Instruments (United Kingdom). The hysteresis curves were recorded at room temperature and the maximum applied magnetic field was 15 kOe.

The structural characterization of Fe_3O_4 nanoparticles was carried out using the X-ray diffraction (XRD) technique. The analysis was performed with an INEL Equinox 3000 diffractometer, which is equipped with a curved multidetector covering 90° in 2θ. This setup enabled the simultaneous acquisition of the complete XRD pattern within the range of 20 to 110°. The characteristic wavelength of Co Kα radiation (λ = 1.7903 Å) was used for the measurements. For these studies, the nanoparticles were lyophilized immediately after synthesis using a Biobase BK-FD 10 Series Vacuum Freeze Dryer (China), which was pre-cooled to −60 °C and operated at a vacuum degree of less than 10 Pa. This process was undertaken to preserve their structural and magnetic properties. The nanoparticles were then analyzed in their dry form, as obtained post-lyophilization.

The absorption spectra of water and the extinction spectra of the magnetic nanoparticles were measured with the V-760 UV-vis-NIR spectrophotometer from Jasco International Co., Ltd (Tokyo, Japan), using 2 mm quartz glass cuvettes from Hellma (Germany).

Magnetic resonance relaxometry. A series of samples were prepared with magnetic nanoparticles dispersed in water and in agarose phantoms. A similar series were prepared but the produced magnetic nanoparticles were replaced with Gadovist, the commercially available contrast agent. The samples (1 mL) were transferred into an NMR tube with 10 mm diameter and measured using a 20 MHz Bruker Minispec relaxometer (Massachusetts, USA). The standard CPMG pulse sequence was applied with an (adjusted) echo time between 70 μs and 2 ms. A number of 3000 echoes were acquired with 64 scans and 3 s recycle delay, to ensure a good signal-to-noise ratio. The CPMG echo train decays were analysed by inverse Laplace transform and the distribution of transverse (spin–spin) relaxation time, T_2, was obtained.

2.5 Photothermal assay

To evaluate the heating capacity and indirect penetration depth of the newly synthesized magnetic nanoparticles, we utilized agarose-based phantoms containing nanoparticles at a concentration of 1.7 μM. These phantoms were placed in centrifuge tubes and irradiated with LED sources detailed in Table 1, sourced from Thorlabs (New Jersey, United States), and adjusted for power using a meter. Irradiation was conducted for 15 minutes, with thermal imaging captured every 30 seconds using an Optris PI 450 infrared camera (Germany). Additionally, to explore the effect of varying concentrations and to study the thermal behavior and efficacy of two distinct irradiation sources, phantoms with different concentrations of nanoparticles (0.1, 3.5, 6.9, 13.8, and 27.6 μM) were irradiated using a 970 nm LED and a 980 nm laser (OBIS 980 nm LX 150 mW LASER SYSTEM) from Coherent (Pennsylvania, United States) set to a power of 100 mW, with each session lasting 15 minutes and thermal images captured at similar intervals (Fig. 1).

Table 1 Specifications of the LEDs used

LED wavelength (nm)	Part number	Bandwidth (FWHM) (nm)	Total beam power (mW)	Experimental power applied (mW)
850	M850L3	30	900	100
970	M970L4	60	720	
1100	M1100L1	50	252	

Control phantoms without nanoparticles were also included to benchmark the results. All experimental conditions were replicated three times to confirm the consistency and reliability of the results.

In addition, the photothermal conversion efficiency (η) of the magnetic nanoparticles irradiated with all 3 LED sources was calculated using the following formula:[19]

$$\eta = \frac{h \cdot s \cdot (T - T_{surr}) - Q_0}{P(1 - 10^{-A_\lambda})} \quad (2)$$

where h is the heat transfer coefficient, s the area cross section of irradiation, T the solution temperature, T_{surr} the ambient surrounding temperature, Q_0 the heat generated by the control under irradiation, P the power of the irradiation source and A_λ the absorption intensity at the excitation wavelength. To estimate Q_0, the specific heat capacity of the agarose phantom was approximated to that of water, considering that it is predominantly of aqueous composition. Eqn (2) also accounts for the correction related to the extinction (A_λ) of the magnetic nanoparticles, as illustrated in Fig. S1.

2.6 Magnetic resonance imaging techniques

11.7 Tesla preclinical MRI system procedures. Three selected samples of agarose-based phantoms with different concentrations of magnetic nanoparticles – 0 (as control), 0.1 and 3.5 μM – placed in 2 mL Eppendorf tubes were introduced in an 11.7 T magnetic field of Bruker BioSpec tomograph. After the initial localization protocols, specific longitudinal (T_1) and transverse (T_2) relaxation time-based sequences were implemented.

1.5 Tesla clinical system procedures. MRI was performed using a Siemens Magnetom Altea clinical scanner operating at 1.5 T. For T1-weighted imaging, a turbo spin echo sequence was utilized with a matrix size of 320 × 224 and a field of view (FOV) of 230 × 230 mm. Axial slices were acquired with a thickness of 2 mm, employing a repetition time (TR) of 2000 ms and an echo time (TE) of 11 ms. For T2-weighted imaging, a turbo spin echo sequence was also used, with a matrix size of 320 × 288 and the same FOV (230 × 230 mm). Axial slices were obtained with a thickness of 3 mm, using a repetition time (TR) of 10 000 ms and an echo time (TE) of 111 ms.

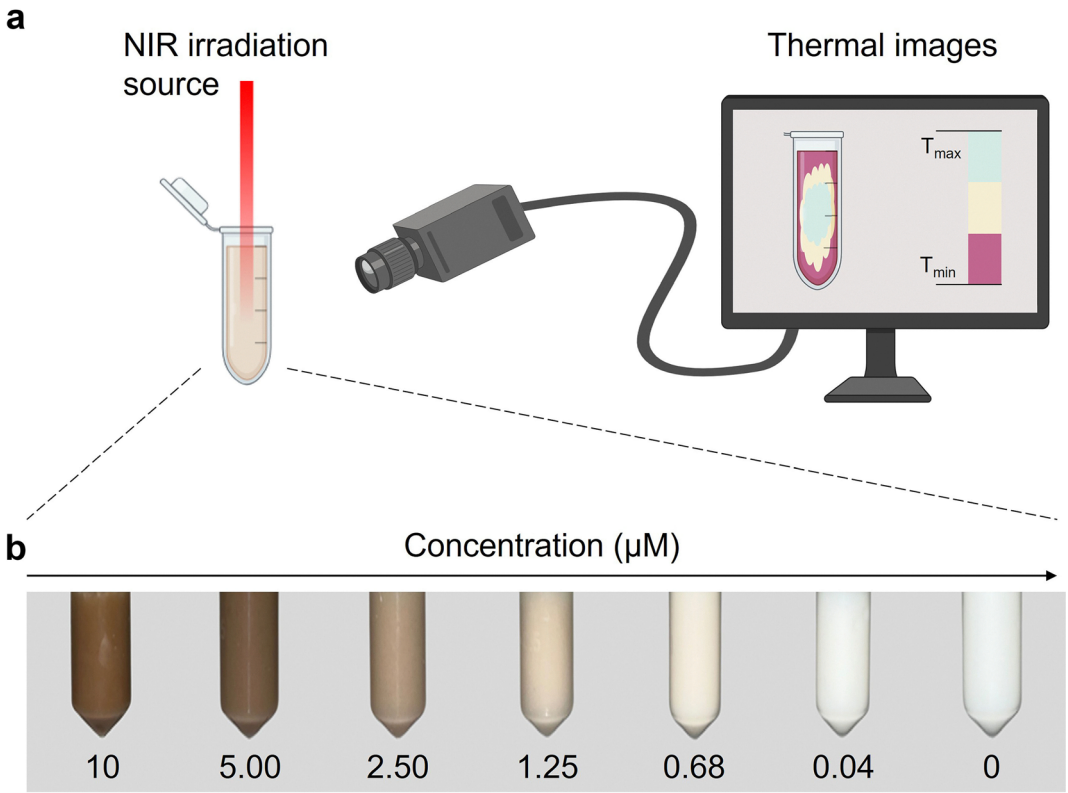

Fig. 1 (a) Schematic representation of the NIR irradiation setup used to assess the thermal response of magnetic nanoparticles within agarose-based phantoms; (b) digital photographs of agarose-based phantoms containing varying concentrations of magnetic nanoparticles. Created with BioRender.com.

3. Results and discussion

3.1 Structural and magnetic characterization

The TEM image depicted in Fig. 2a illustrates magnetic nanoparticles which display typical behavior of clustering due to their magnetic properties. This clustering is observed when the particles are dried and is a physical characteristic resulting from the magnetic nature of the nanoparticles, rather than a sign of aggregation or instability.

The accompanying histogram (Fig. 2b) provides a quantitative analysis of their sizes, with most nanoparticles measuring between 5 and 25 nm. The size distribution, assessed using the minimum Feret diameter, has a mean of 9.23 ± 2.97 nm across more than 1600 analyzed nanoparticles. This mean diameter suggests that the majority of individual nanoparticles are quite small, indicating a fine dispersion of particles when in suspension.

Next, the zeta potential of our newly synthesized magnetic nanoparticles was measured at 31.6 ± 1.8 mV, indicating a relatively high degree of surface charge stability. This positive value suggests strong electrostatic repulsion between particles in suspension, which enhances their colloidal stability. At lower concentrations, this repulsion helps maintain dispersion, while

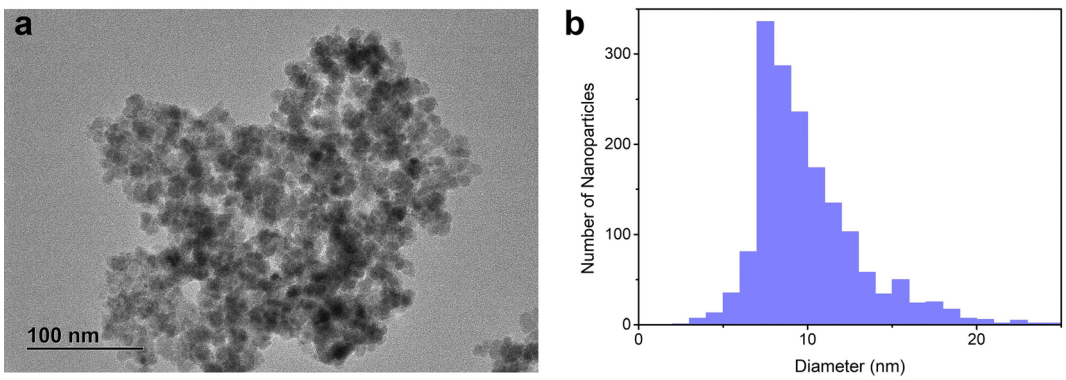

Fig. 2 (a) TEM image of magnetic nanoparticles, with a scale bar of 100 nm. (b) Histogram of particle size distribution measured by using the minimum Feret diameter.

at higher concentrations, the magnetic properties may lead to aggregation due to increased particle interactions. Such stability is crucial for maintaining consistent properties and behavior in physiological environments.

To further evaluate colloidal behavior in suspension, we conducted DLS measurements at various concentrations in both ultrapure water and fetal bovine serum (FBS). In water, the nanoparticles exhibited clear signs of concentration-dependent aggregation, with hydrodynamic diameters decreasing from 1207 ± 73 nm at 1.8 μM to 788 ± 88 nm (85%) and 260 ± 127 nm (15%) at 0.6 μM, and down to 351 ± 65 nm at 0.06 μM (see Table S1). This behavior reflects the interplay between magnetic dipole interactions and electrostatic repulsion, with higher particle proximity at increased concentrations favoring clustering.

To complement the morphological and hydrodynamic analysis in water, we further investigated the nanoparticle behavior in the biologically relevant medium FBS, by performing DLS measurements. This protein-rich medium better mimics the *in vivo* conditions of blood plasma, offering insight into potential dispersion behavior under physiological conditions. In contrast to water, where the nanoparticles displayed significant and concentration-dependent aggregation, their behavior in FBS revealed markedly enhanced colloidal stability. At 1.8 μM, a single, well-defined population was detected at 508 ± 47 nm, and even at lower concentrations (0.6 and 0.06 μM), the system remained more homogeneous (Table S2). Notably, minor populations at ~6 nm were consistently observed at these lower concentrations, likely corresponding to nanoparticles in their monomeric, unaggregated form – a feature not observed in water (Fig. S3).

These differences are likely driven by the formation of a protein corona in FBS, which can shield surface charges and prevent magnetic dipole interactions, thus reducing aggregation. Additionally, the higher viscosity and ionic strength of FBS further contribute to stabilizing the dispersion. The comparison highlights that aggregation observed in water is not an intrinsic limitation of the nanoparticles themselves but rather a consequence of the dispersion medium. These findings support the idea that, under realistic biological conditions, the nanoparticles are much more likely to remain well-dispersed, especially when combined with surface functionalization strategies planned for future biomedical applications.

In general, iron oxide nanoparticles, composed of iron(II) and iron(III) oxides, typically manifest as magnetite (Fe_3O_4) and maghemite (γ-Fe_2O_3) in varying proportions. Magnetite is generally favored for its robust magnetic properties, though it is susceptible to oxidation, resulting in the formation of maghemite.[20] X-ray diffraction (XRD) is a critical technique for evaluating the crystalline structure, crystallite size, phase, and lattice parameters of these nanoparticles.[21] After initially determining the size range and zeta potential of the synthesized nanoparticles, XRD analysis was undertaken to define their crystalline nature.

Thus, the XRD pattern of the nanoparticles prepared is shown in Fig. 3a. A series of XRD peaks is observed, characterized by relatively large full width at half maximum (FWHM) and low intensities, which are typical features of nanostructured materials. According to the JCPDS 01-075-0449 file, all observed peaks correspond to the cubic spinel structure of Fe_3O_4. The high degree of crystallinity of the produced particles is evidenced by the observation of even low-intensity XRD peaks, such as the (642) reflection, which has a theoretical intensity of 2.2%. Within the detection limits of the XRD technique, no secondary phases were identified. Thus, we can conclude that the experimental method employed in this study successfully produced single-phase Fe_3O_4 nanoparticles.

The average crystallite size (D) of the synthesized nanoparticles can be determined from the XRD data, using the Debye–Sherrer equation:[22]

$$D = \frac{k\lambda}{\beta \cos\theta} \tag{3}$$

where λ = 1.7903 Å is the wavelength corresponding to the XRD instrument, k = 0.9 is a constant and β is the full width at half maximum of the five most intense diffraction peaks. The diffraction pattern of a reference sample was used to determine the resolution of the diffractometer and to have access to the real value of the β parameter.

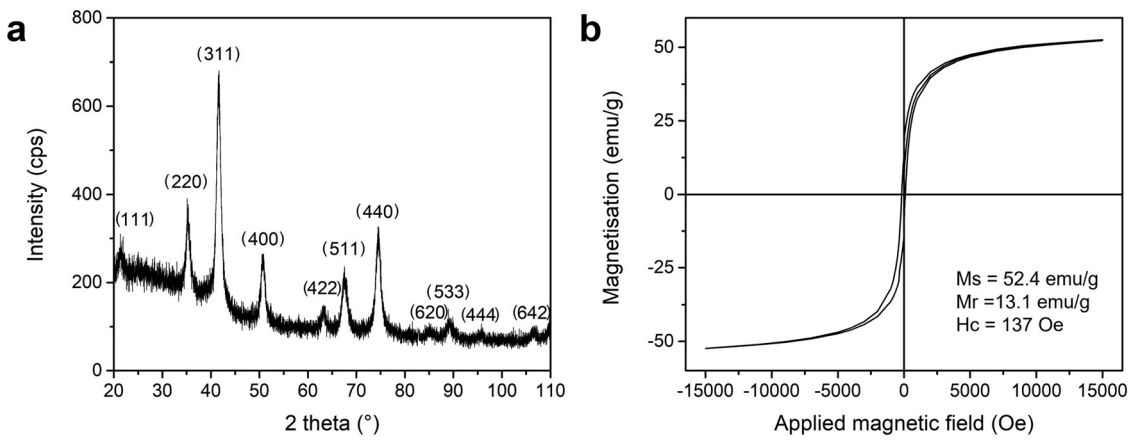

Fig. 3 Structural and magnetic characterization of the Fe_3O_4 nanoparticles. (a) XRD pattern and (b) magnetization curve of the prepared powders.

Using eqn (3), the average crystallite size of the magnetic nanoparticles was determined to be 10.3 ± 2 nm. The close agreement between the particle size estimated from TEM (9.23 ± 2.97) and the crystallite size calculated from XRD (10.3 ± 2 nm) strongly suggests that the synthesized Fe_3O_4 nanoparticles are predominantly monocrystalline. This indicates that each nanoparticle consists of a single crystalline domain without significant grain boundaries, which is advantageous for maintaining uniform magnetic properties and efficient energy transfer in biomedical applications. The monocrystalline nature minimizes structural defects, potentially reducing magnetic anisotropy and enhancing superparamagnetic behavior, which is critical for MRI contrast enhancement.

Hysteresis curves are fundamental for characterizing the magnetic properties of materials, particularly nanoparticles like Fe_3O_4. These curves provide insights into the material's magnetic behavior under an applied magnetic field, allowing researchers to determine key properties such as saturation magnetization (M_s), remanence, and coercivity.[23] Such measurements are crucial for assessing the suitability of magnetic nanoparticles for various applications, including MRI contrast agents, drug delivery systems, and hyperthermia cancer treatment.

The hysteresis curve of our newly synthesized nanoparticles is shown in Fig. 3b. The shape and characteristics of the curve are typical of soft ferrimagnetic materials. The M_s of the prepared particles is 52.4 emu g^{-1}, which aligns with values reported in the literature for Fe_3O_4 nanoparticles. For example, M. Anbarasu *et al.* produced Fe_3O_4 nanoparticles *via* the coprecipitation method, reporting saturation magnetization values in the range of 51–62 emu g^{-1}.[24] Similarly, L. F. Gomez-Caballero *et al.* reported saturation magnetization values for Fe_3O_4 nanoparticles between 55 and 62.3 emu g^{-1}.[25]

Considering the nanometric size of our newly prepared nanoparticles, we initially expected superparamagnetic behavior. However, according to the vibrating sample magnetometer (VSM) analysis, this was not observed, as the particles exhibit remanence and coercivity. The coercivity value obtained for our samples is consistent with values reported in the literature for Fe_3O_4 nanoparticles with larger diameters. For instance, M. D. Nguyen *et al.* reported coercivity values between 115 and 149 Oe for nanoparticles with diameters ranging from 82 to 188 nm.[26] We attribute the absence of superparamagnetic behavior in our particles to nanoparticle agglomeration. This phenomenon, caused by dipole–dipole interactions, has been previously reported in the literature, with studies highlighting that such agglomeration can suppress superparamagnetic behavior.[27]

Next, the yield of the synthesized magnetic nanoparticles exhibited variability, with a mean of 52.83% and a standard deviation of 9.20%. This indicates a moderate variation in synthesis efficiency, which is a common occurrence in batch-to-batch productions. Such differences in yield can be attributed to multiple factors, including the rigorous washing protocol employed. The nanoparticles were washed six times to eliminate all CTAB, a process essential for preventing the formation of CTAB crystals during drying, which could potentially lead to inaccuracies in mass determination. However, this intensive washing likely led to some losses of nanoparticles during the removal of the supernatant, impacting the overall yield.

XRD analysis confirmed the identity of the product as Fe_3O_4, known to have a molecular mass of 231.533 g mol^{-1}. By calculating the yield and validating the composition of the nanoparticles, we determined the molar concentration of our aqueous nanoparticle solution. This precise concentration was critical for ensuring consistent experimental conditions in subsequent studies, facilitating reliable comparisons and enhancing the reproducibility of the results. The standardized molar concentration was utilized in further investigations, exploring the nanoparticles' photothermal and magnetic properties.

3.2 Photothermal properties assay in tissue-mimicking phantoms

Recent advancements in hyperthermia treatments for tumors have increasingly focused on the application of NIR irradiation and magnetic nanoparticles. The localized heating produced by magnetic nanoparticles exposed to NIR radiation could be facilitated by d–d electron transitions or the transfer of electrons from the conduction band to the valence band.[28] This phenomenon has been the subject of numerous studies, elucidating the behavior of magnetic nanoparticles under NIR irradiation in aqueous solutions. For instance, Bilici *et al.* demonstrated the use of magnetic nanoparticles as thermal agents in photothermal therapy (PTT), employing a 785 nm laser with an output of 800 mW, which achieved a temperature increase of 12.8 °C after 20 minutes.[29] However, it is crucial to note that the power levels often employed in such studies exceed the maximum permissible exposure (MPE) recommended by the International Commission on Non-Ionizing Radiation Protection (ICNIRP) and the American National Standards Institute (ANSI), potentially leading to photodamage in adjacent healthy tissues due to the high intensity and prolonged exposure times. Typically, NIR radiation safety guidelines suggest an MPE of 0.1, and up to 0.3 W cm^{-2} for exposures longer than 10 seconds, aimed at mitigating thermal injury risks.[30,31]

Furthermore, the physical context in which these magnetic nanoparticles are studied significantly influences their thermal efficiency. Notably, Kaczmarek *et al.* demonstrated that magnetic nanoparticles generate heat more effectively in fluid, where their movement is unrestricted, compared to more stationary environments like tissues, which exhibit a lower temperature rise. This research, primarily conducted in magnetic fields, highlights the variability in thermal responses depending on the environment. It underscores the importance of employing gel-based phantoms, such as agarose, to simulate tissue-like conditions for more accurate assessment of heat distribution. This phenomenon of enhanced thermal efficiency in fluid media is relevant irrespective of the excitation source, suggesting that the findings can be extrapolated to photothermal excitation scenarios.[32]

In this context, we evaluated the thermal properties of newly synthesized magnetic nanoparticles under light irradiation in phantom-like environments, an approach that mirrors potential clinical settings. To the best of our knowledge, this is among the first studies to specifically investigate NIR-induced thermal

behavior originating from the magnetic core itself (Fe_3O_4), rather than from additional photothermal agents integrated into the nanoparticle structure, within a tissue-mimicking environment.

Heating evaluation by the NIR wavelength source. One of the main goals of our study was to indirectly investigate the penetrative capability and thermal performance of magnetic nanoparticles under irradiation by different NIR LEDs, analyzing how different wavelengths influenced these properties. The wavelengths used were 850, 970, and 1100 nm, and the emission profiles of these LEDs in relation to water's inherent absorption characteristics are displayed in Fig. 4a.

The penetration depths achieved by the nanoparticles varied significantly with wavelength (Fig. 4b). Under 850 nm LED irradiation, the nanoparticles achieved a penetration depth of approximately 1.4 cm, while at 970 nm, this depth increased notably to 2.1 cm, marking the highest penetration among the tested wavelengths. Conversely, the 1100 nm LED showed a similar penetration depth to the 850 nm LED at about 1.3 cm. This variation can be attributed primarily to the different absorption characteristics of water within these NIR ranges (see Fig. S2, thermal images of control phantoms without nanoparticles under NIR irradiation), as highlighted in the provided spectral data where water shows distinct absorption peaks. Particularly, the 970 nm wavelength aligns closely with a notable but relatively less intense water absorption peak, as detailed by Curcio and Petty,[33] which may explain its deeper penetration capability compared to the more intensely absorbed neighboring wavelengths. This strategic position allows for more effective transmission through the phantom, minimizing absorption by the water itself and enhancing the interaction with the embedded nanoparticles.

Thermal responses of the phantoms, both those embedded with magnetic nanoparticles and the control (water-based), were carefully monitored. At 850 nm, the nanoparticle-embedded phantom exhibited a temperature rise of 3.0 °C, while the control phantom's temperature increased by 0.5 °C. The 970 nm LED, which achieved the deepest penetration, resulted in a temperature increase of 5.0 °C for the nanoparticle phantom and 1.9 °C for the control, highlighting the superior energy absorption capabilities of the nanoparticles. Similarly, under 1100 nm LED irradiation, the nanoparticle phantom showed a temperature increase of 2.8 °C, compared to 2.0 °C for the control.

The observed thermal behaviors across different wavelengths underscore the complex interplay between water absorption properties and the specific resonance characteristics of the nanoparticles. Interestingly, although the 970 nm wavelength is near a region of significant water absorption, it facilitated the most effective heating and penetration. This suggests that the nanoparticles are particularly tuned to this wavelength, enhancing their energy conversion efficiency despite the competitive absorption by water. In contrast, at 850 and 1100 nm, where water absorption is less significant relative to that at 970 nm, the thermal responses were less pronounced. Therefore, for applications involving photothermal therapy with these particular nanoparticles, the 970 nm wavelength emerges as the most effective, offering a balance between deep tissue penetration and efficient thermal conversion, critical for achieving therapeutic efficacy.

This detailed understanding of wavelength-dependent interactions within NIR irradiated systems is crucial for optimizing the application of magnetic nanoparticles in therapies such as photothermal treatment, where controlled heating and precise depth targeting are required. The choice of 970 nm for deeper tissue penetration could be particularly beneficial in medical applications targeting deeper-seated tissues, while understanding the absorption properties of the medium (water in this case) helps in tailoring the nanoparticle properties and irradiation conditions for optimal therapeutic outcomes.

Photothermal conversion efficiency. This study is the first to investigate Fe_3O_4 magnetic nanoparticles as sole photothermal agents under NIR irradiation within tissue-mimicking phantoms, bridging the gap between *in vitro* solution tests and realistic tissue conditions. In our experiments, magnetic nanoparticles were embedded in 3D agarose phantoms doped with optical scatterers and absorbers to simulate the light

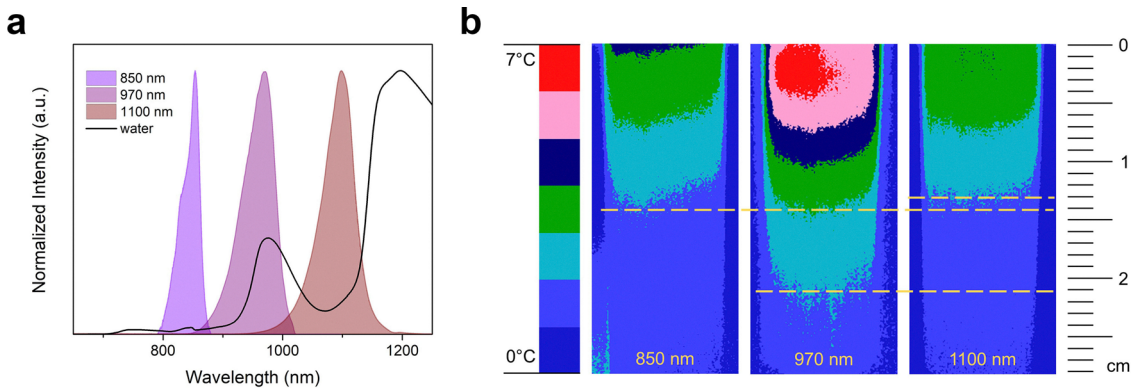

Fig. 4 (a) Emission profiles of NIR LED irradiation at a wavelength of 850, 970, and 1100 nm, compared with the absorption spectrum of water; (b) thermal and indirect penetration effects in phantoms with magnetic nanoparticles (concentration of 1.7 μM) under NIR LED irradiation at 850, 970, and 1100 nm. The color scale indicates the temperature reached after 15 minutes of irradiation, while the dotted lines show the depth of penetration in phantoms.

attenuation of biological tissue.[34] This phantom-based approach is novel for PTT with magnetic nanoparticles; previous studies typically measured photothermal heating in clear aqueous suspensions or cell cultures,[35,36] which do not account for the significant scattering and absorption that occur in real tissue. The η we obtained for magnetic nanoparticles under NIR irradiation sources (850 nm – η = 45.12%; 970 nm – η = 71.59%; 1100 nm – η = 16.76%) falls within the broad range reported in the literature for iron oxide nanostructures.[19,36–55] In general, η values for Fe_3O_4 are highly dependent on experimental conditions and nanoparticle design, spanning from only a few percent in basic colloidal systems up to tens of percent in optimized formulations. For instance, one study found that poly(acrylic acid)-stabilized Fe_3O_4 (around 10 nm) achieved ~76% efficiency, vastly outperforming larger aggregated Fe_3O_4 in polymer beads (28–34%) or uncoated particles (~16%).[36] Such enhancements were attributed to better dispersion and higher surface area in the small, well-stabilized nanoparticles.

Reported η values also vary with excitation wavelength and source: Fe_3O_4 tends to absorb NIR light less efficiently at longer wavelengths, so lasers in the first biological window (~808 nm) often induce higher η compared to those in the second window (~1064 nm). For example, Peng *et al.* observed that transferrin/TAT-functionalized Fe_3O_4 had an η of ~37% under 808 nm irradiation,[49] while Huang *et al.* reported ~20.8% efficiency for clustered magnetite under a 1064 nm laser.[56] Similarly, 785 nm excitation can yield higher η (~56%) for Fe_3O_4 than 808 nm (~42%) in comparable nanoparticle systems,[36] highlighting the influence of the material's absorption profile. In contrast, using a broad-spectrum excitation (such as solar illumination) can push the apparent efficiency even higher – one Fe_3O_4-based nanofluid showed ~93% solar-to-heat conversion[57] – although such conditions differ from the narrow-band NIR lasers used in PTT. To compare the performance of the magnetic nanoparticles developed in this work, a literature review was conducted to compile data on capping/coating agents, nanoparticle concentrations, sizes, photothermal conversion efficiencies, and irradiation sources reported in studies investigating the photothermal effects of magnetic nanoparticles under NIR irradiation. This information is summarized in Table S3 in the SI.

Overall, the η measured in our tissue phantom study aligns with these literature values, confirming that our Fe_3O_4 nanoheaters achieve comparable efficacy within the expected range even under the more stringent, tissue-like conditions.

Heating evaluation by the concentration of magnetic nanoparticles. Building on the findings focused on the effectiveness of different NIR wavelengths, we now extend our investigation to compare the thermal behavior and efficacy of two closely matched irradiation sources: a 970 nm LED and a 980 nm laser. This comparison aims to discern whether the type of light source – LED *versus* laser – significantly influences the outcomes.

Additionally, acknowledging the critical role of nanoparticle concentration in achieving desired therapeutic outcomes, we will systematically vary the concentration of magnetic nanoparticles within the phantoms. By exploring a broad range of concentrations, we aim to simulate different scenarios related to how these nanoparticles may distribute within the body, interact with various tissues, and how their concentration affects the timing and quality of interventions. This comprehensive approach will allow us to identify the optimal concentration that maximizes therapeutic effectiveness while accommodating the dynamic nature of nanoparticle behavior in biological systems. Such detailed investigations are crucial for tailoring the use of nanoparticles to specific patient conditions, ensuring enhanced safety and efficacy in real-world clinical scenarios.

The thermal images presented in Fig. 5a, captured at the 15-minute mark for both LED and laser irradiation across all concentrations, reveal significant insights into the depth of penetration of the heat within the phantoms. These images show that LED irradiation achieves deeper penetration into the phantom compared to the laser. Furthermore, the penetration depth varies with the concentration of the nanoparticles, with higher concentrations resulting in deeper penetration. This variation underscores that the indirect penetration depth is influenced not solely by the water absorption characteristics, but also significantly by the thermal effects generated by the nanoparticles themselves. This observation affirms the critical

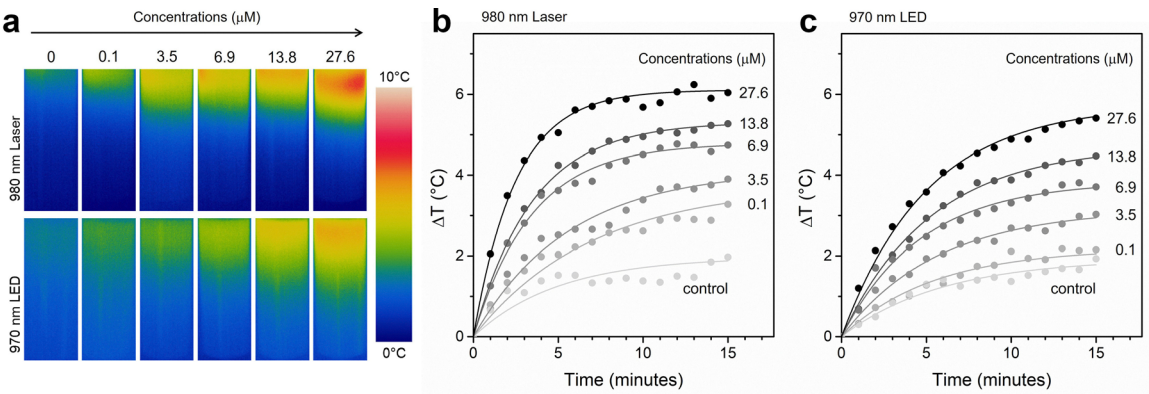

Fig. 5 (a) Thermal images after 15 minutes of irradiation, (b) temperature profiles for a 980 nm laser, and (c) temperature profiles for a 970 nm LED. All panels display phantoms containing magnetic nanoparticles at concentrations from 0 to 27.6 μM, illustrating both thermal distribution and the temperature change over time.

role of nanoparticle-mediated heat generation in enhancing the efficacy of photothermal therapies, highlighting the importance of nanoparticle concentration in optimizing therapeutic outcomes.

Moreover, the temperature profiles depicted in the plots (Fig. 5b and c) clearly illustrate that the increase in temperature within phantoms embedded with magnetic nanoparticles is directly proportional to the nanoparticle concentration. Notably, under laser irradiation, the temperature rise was rapid, achieving a peak at about 5 minutes, whereas the LED-induced temperature increase was more gradual, reaching its peak only after 15 minutes of exposure. Despite these differences in the rate of temperature increase, the maximum temperature achieved for both irradiation sources was approximately 6 °C at the highest nanoparticle concentration (27.6 μM). This observation highlights that while the rate of heating differs between the two sources, the ultimate thermal capacity at this concentration remains consistent. This distinction in heating dynamics emphasizes the importance of selecting an appropriate irradiation source based on the desired rate of temperature increase for specific applications.

In our experiments, the thermal response observed using a 970 nm LED and a 980 nm laser as excitation sources achieved mild hyperthermia conditions with nanoparticle concentration as low as 3.5 μM. This underscores the potential of these methods to enhance therapeutic outcomes without causing excessive damage to surrounding healthy tissues. Mild hyperthermia typically involves heating tissues to temperatures between 39 and 45 °C, with the lower threshold of this range (around 39 °C) being critical to initiate biological benefits such as increased blood flow, enhanced oxygenation, and heightened cellular metabolism. These benefits are essential for effective treatment integration with therapies like chemotherapy or radiation. Operating within this temperature range not only ensures optimal therapeutic efficacy but also minimizes cellular damage that could result from higher temperatures.[58–60] Precise temperature control is crucial for achieving the desired therapeutic impact without adverse effects, where NIR wavelengths are advantageous due to their minimal scattering and absorption in physiological tissues.

3.3 Magnetic resonance relaxometry

Typically, Gadovist, a Gd-based contrast agent commonly used in MRI, is administered at a concentration of 0.1 mmol kg^{-1}, which for an adult weighing 70 kg results in a total of 7 millimoles. Given that a 70 kg person has about 5 liters (5000 mL) of blood, the molar concentration of Gadovist in the bloodstream would initially be approximately 0.0014 mmol mL^{-1} (1.4 μM). This assumes even distribution throughout the blood, but in practice, the contrast agent can also distribute into other organs or concentrate more in specific regions. Additionally, the concentration can vary depending on the timing of the MRI relative to the administration of the agent. Therefore, it is crucial to study a range of concentrations, recognizing that the actual distribution and concentration *in vivo* can differ significantly from this initial calculation.

Thus, in order to assess the efficiency of our magnetic nanoparticles as contrast agents in MRI, the effect of concentration must be evaluated and compared to a clinically approved contrast agent, *i.e.*, Gadovist. The T_2 distributions measured for Gadovist (1 mmol mL^{-1}) and magnetic nanoparticles dispersed in distilled water or ultrapure water, at various concentrations, are presented in Fig. 6. The distilled water shows a single peak located at the most probable T_2 value of 2.91 s, as seen in the gray T_2 distribution at the bottom of Fig. 6a. A solution containing Gadovist in distilled water at a final concentration of 10 μM presents a significant contrast effect, seen as a large shift in the T_2 distribution to a T_2 value of 7.9 ms (see the black distribution on top of Fig. 6a). The other solutions were obtained by successively halving the Gadovist concentration down to 0.01 μM Gadovist. The decay of T_2 values with increasing Gadovist concentration is shown in Fig. 6c.

Single peaks are measured for the clear and uncolored solution of Gadovist; however, this is no longer the case for magnetic nanoparticle solutions. The ultrapure water presents a transverse relaxation time T_2 of 2.56 s (see the gray T_2-distribution in Fig. 6b), which decreases with the increasing concentration of magnetic nanoparticles. Additionally, starting with a concentration of 0.005 μM, small peaks accompany the main peak. Thus, the main peak (with the largest integral area) contains ultrapure water with fully dispersed magnetic nanoparticles, while the smaller peaks at lower T_2 values can be associated with clusters of magnetic nanoparticles of varying sizes (see Fig. 2), which are not fully dispersed and interact with a layer of water molecules up to an effective action distance. The T_2 values of the peaks (position of the peak in the T_2 distribution) may indicate the size of the magnetic nanoparticle cluster. Smaller clusters, being more mobile, are characterized by larger T_2 values, while larger clusters, being less mobile, are characterized by smaller T_2 values. Fig. 6b shows that the sizes of magnetic nanoparticles are relatively small up to a concentration of 0.04 μM. Starting with a concentration of 0.08 μM, the amount of water molecules interacting with undispersed magnetic nanoparticles increases significantly (see the peak located at T_2 = 57.2 ms – green T_2-distribution in Fig. 6b). For magnetic nanoparticles of 0.17 μM concentration, this secondary peak becomes significant. For this reason, the T_2 distributions are presented for solutions with this maximum concentration. More concentrated solutions of magnetic nanoparticles (similar to those used for Gadovist) were measured (not shown) but they presented large secondary peaks interpreted as complex magnetic interactions within the clusters of magnetic nanoparticles, making them unsuitable for use as contrast agents.

It is important to emphasize that these measurements in water do not imply that the nanoparticles are inefficient at higher concentrations in general. Instead, the apparent drop in performance at elevated concentrations is likely due to the tendency of Fe_3O_4 nanoparticles to aggregate in ultrapure water, which interferes with relaxivity by inducing magnetic coupling effects. This aggregation is a known artifact in aqueous suspensions and not representative of physiological conditions. To address this, additional measurements were conducted in agarose-based phantoms that better simulate

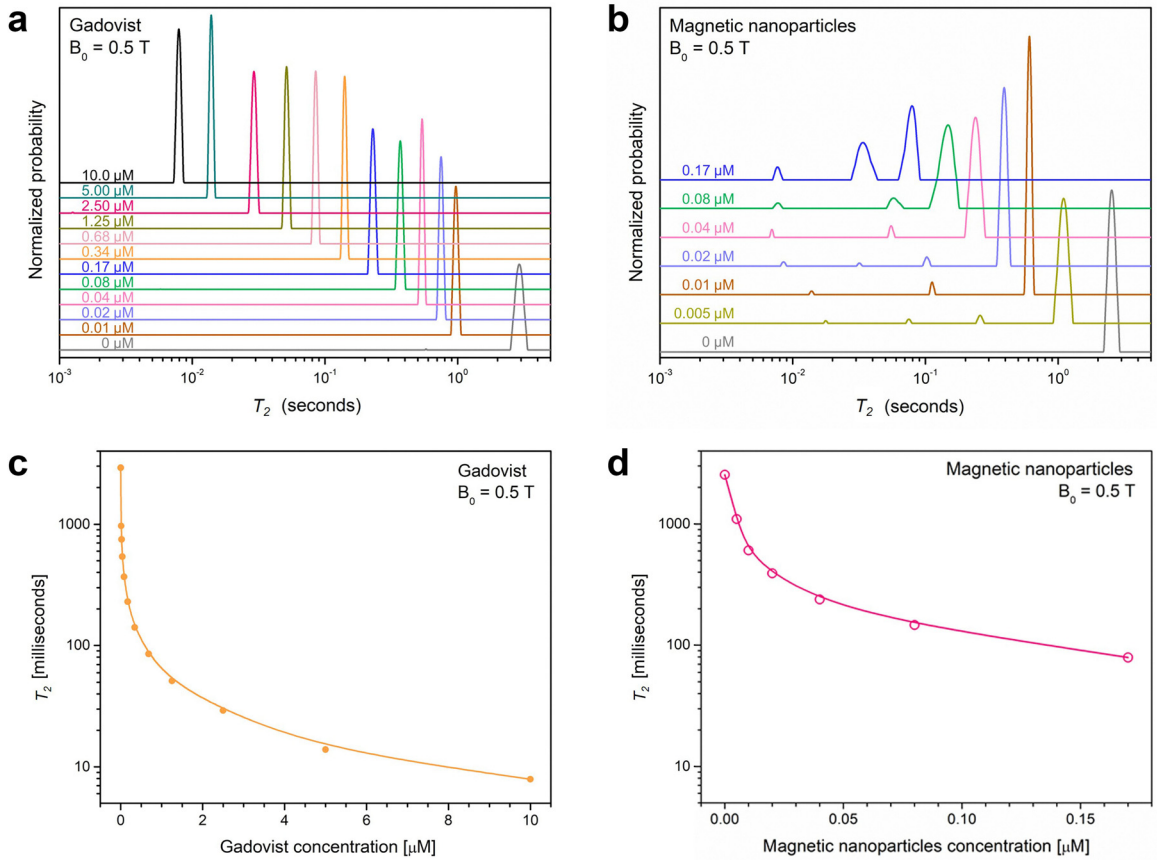

Fig. 6 Distributions of transverse relaxation time T_2, measured for various water solutions with different concentrations of (a) Gadovist and (b) magnetic nanoparticles and the decay curve of the main peak as a function of (c) Gadovist and (d) magnetic nanoparticle concentration.

the tissue microenvironment. Moreover, as shown in the DLS analysis included in the SI (Fig. S3), the nanoparticles exhibit significantly reduced aggregation in FBS compared to water. This suggests that in biological media – more representative of *in vivo* conditions – the particles remain more dispersed and could retain high MRI efficiency even at larger concentrations.

The decay of main T_2 values (measured for the main peak characterized by the large integral area associated with water interacting with fully dispersed magnetic nanoparticles) as a function of magnetic nanoparticle concentration is presented in Fig. 6d. Comparing the decay of T_2 values using the commercial contrast agent (*i.e.*, Gadovist) with the decay of T_2 values using the magnetic nanoparticles, one can see that the newly synthesized magnetic nanoparticles are competitive (with Gadovist) in the domain of low concentration. This decay, by an order of magnitude, is sufficient to induce a visible effect in MRI images. While the magnetic nanoparticles are more biologically friendly (compared to Gadovist), they may exhibit clustering effects at higher concentrations in pure water, which can reduce relaxivity. However, such behavior is strongly medium-dependent and was not observed to the same extent when studied in FBS (see Fig. S3), suggesting that under physiological conditions, the particles may remain more stable and effective.

The previously discussed results reflect contrast behavior in fluid environments (such as blood). However, once contrast agents cross barriers like the BBB and enter tissue, their interaction dynamics change significantly. To simulate the mechanical consistency of tissue, we employed agarose-based phantoms, which better replicate the reduced mobility of protons in biological matrices such as fatty lipids. A series of samples with different concentrations of Gadovist and magnetic nanoparticles dispersed in agarose-based phantoms were prepared and measured. Due to the high viscosity of the samples, in order to transfer them into the NMR tube, they were first placed into a 0.5 mL centrifuge tube and then, using this vehicle, slid into the bottom of the NMR tube. An empty tube was also measured as control and was found to have a relatively large peak located at a T_2 value of approximately 50 μs (which is usually filtered out in the measurements of phantoms) and two other minor peaks located at 1.06 ms and 5.74 ms. These two peaks can be observed in the gray T_2 distribution (bottom in Fig. 7a and b) obtained for agarose-based phantoms with no magnetic nanoparticles. As expected, the contrast agent effect of both Gadovist and magnetic nanoparticles, evaluated as the decay of T_2 values with the increasing concentration of the contrast agent, is much reduced in phantoms. This is due to the fact that the ^{1}H sourced from agarose molecules is significantly less mobile. Initially, one can observe that the reference T_2 value (2.56 s for ultrapure water or 2.91 s for distilled water) is already 61 ms as measured for the

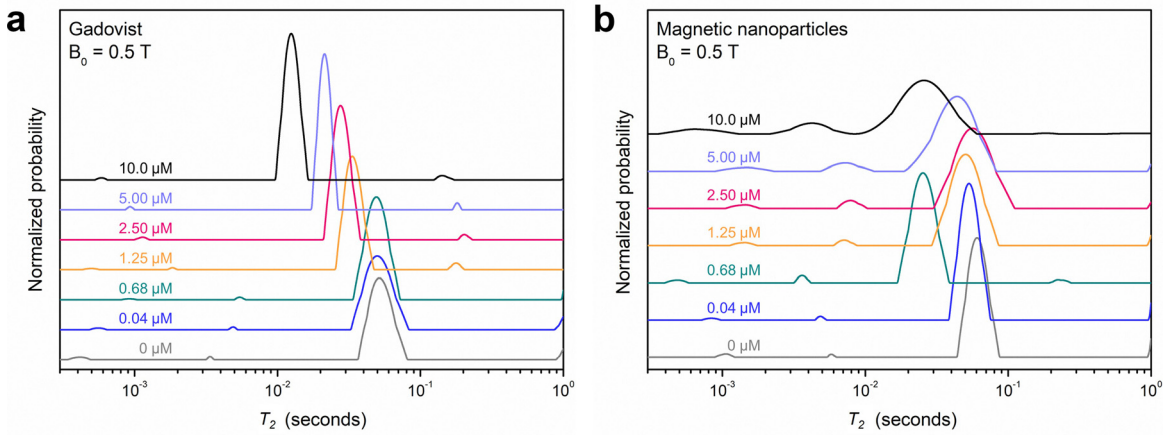

Fig. 7 Distributions of transverse relaxation time T_2, measured for various agarose phantoms with different concentrations of (a) Gadovist and (b) magnetic nanoparticles.

agarose-based phantom with no contrast agent. From this, one can see (Fig. 7a) a systematic shift in the case of using Gadovist as the contrast agent up to a T_2 value of 12.5 ms for a 10 μM Gadovist solution. This effect is not as pronounced when using magnetic nanoparticles. For instance, a phantom with 1.25 μM magnetic nanoparticles presents the main peak located at T_2 = 50.2 ms. Starting from a concentration of 2.5 μM, the peaks become larger, indicating an increase in heterogeneity, sometimes associated with an increase of the main T_2 value. This indicates that the magnetic nanoparticles begin to interact with each other before the agarose-based phantoms transition from a liquid to a solid state, resulting in compensated magnetization. A certain effect can be observed for concentrations of magnetic nanoparticles higher than 2.5 μM (*i.e.*, 2.5, 5.0 and 10 μM) where the decay of T_2 values is noted. At the same time, the peaks become larger, also indicating an increase of heterogeneity.

In living tissues, a large concentration of a dispersed contrast agent implies a much larger concentration in the blood, which may not always occur in practice. Most probably, the effect of contrast agents observed as the change of color in an MRI image is the combined effect of contrast agents partly found in the blood stream and partly in the tissues. Moreover, this is a dynamic process, with a rapid increase of contrast agent concentration in the blood stream; then part of this will cross the blood–tissue barrier and can be found in tissues in the close vicinity of blood vessels, with the possibility to diffuse in the whole tissue. During this time, the concentration of contrast agents will decay due to filtration and accumulation in tissues (organs). Over a slower process, the contrast agents will also be removed from tissues. Unfortunately, part of this may remain in tissues for a much longer time.

3.4 Magnetic resonance imaging

MRI contrast agents are broadly classified as positive or negative based on their effect on signal intensity, with positive T_1 contrast agents enhancing the signal by reducing the longitudinal T_1 relaxation time. This shortening of T_1 generates hyperintense regions in MR images while also enabling shorter repetition times, thereby increasing the number of scans per unit time. Additionally, T_1 agents provide greater specificity compared to negative contrast markers, as signal loss can arise from various confounding factors, such as air–water interfaces (*e.g.*, bubbles) or endogenous iron accumulation. Magnetic nanoparticles, including commercially available ones like ferumoxytol, exhibit strong T_1 contrast even at subclinical magnetic field strengths, surpassing Gd-based agents in relaxivity and enabling novel low-field MRI techniques.[61]

High-resolution imaging with a 11.7 Tesla preclinical MRI system. In order to test the efficiency of the magnetic nanoparticles as MRI contrast agents in tissue-mimicking environments, *i.e.*, phantoms, a preclinical study was performed. In Fig. 8, a series of 5 images recorded with a time of repetition (time for remagnetization – TR) ranging from TR = 0.49 s to TR = 9.99 s are presented. In Fig. 8c, the specific localization of samples and the magnetic nanoparticle concentration are presented. The images are encoded (weighted) with (i) the longitudinal relaxation time T_1, explored *via* the TR experimental parameter, and (ii) the apparent ^{1}H spin density. All three samples are characterized with a good approximation by the same ^{1}H spin density. Nevertheless, at a large TR value (see Fig. 8e) the specific intensities of the three samples differ significantly.

This effect is due to the strong influence of the transverse relaxation time. All MR images are obtained using the spin echoes, as some periods of time are necessary to accommodate the magnetic field gradients for slice, phase and frequency encoding. In this case the echo time was consistently 6 ms, which was enough to lead to significant decay, especially in the case of the sample with 3.5 μM magnetic nanoparticle concentration. Using the series of T_1 weighted images, the longitudinal time was estimated and was found to be as follows: (i) T_1 = 2.459 s for the agarose-based phantom with no magnetic nanoparticles; (ii) T_1 = 1.47 s for the agarose-based phantom with 0.1 μM magnetic nanoparticles; and (iii) T_1 = 0.71 s for the agarose-based phantom with 3.5 μM magnetic nanoparticles. These data show that, in theory, a concentration of 3.5 μM magnetic nanoparticles significantly reduces the longitudinal relaxation time, but this leads to an

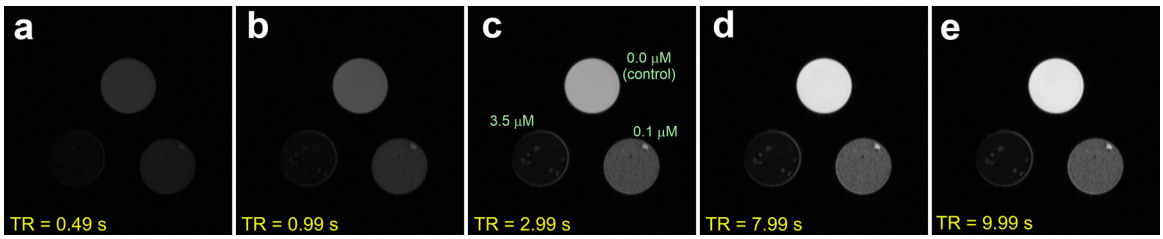

Fig. 8 MR image recorded at 11.7 T magnetic field induction for three agarose phantom samples with 0 (control), 0.1 and 3.5 μM magnetic nanoparticle concentrations, with an echo time TE = 6 ms and different repetition times (time for remagnetization) (a) TR = 0.49 s; (b) TR = 0.99 s; (c) TR = 2.99 s; (d) TR = 7.99 s and (e) TR = 9.99 s exploring the longitudinal relaxation time T_1.

apparent ^{1}H spin density of just 5.87% compared to the ^{1}H spin density of a control phantom. A much smaller concentration of 0.1 μM magnetic nanoparticles leads to an apparent ^{1}H spin density of ∼36%, making it more desirable for practical use. As a side effect, some inhomogeneity inside of the prepared samples can also be observed.

The same strong contrasting effect is also observed in the T_2 weighted images. These are obtained using the T2map-MSME (multi slice multi echo) protocol. In Fig. 9a, a total of 5 images for two slices (no. 2 and 4) were recorded for echo 1 (TE = 6.5 ms), echo 2 (TE = 13 ms), echo 3 (TE = 18.5 ms), echo 5 (TE = 32.5 ms) and echo 10 (TE = 65 ms) and a repetition time TR = 2.6 s. In total, 64 images were recorded, which led to the calculated transverse relaxation time as follows: (i) T_2 = 38.7 ms for the agarose-based phantom with no magnetic nanoparticles; (ii) T_2 = 12.79 ms for the agarose-based phantom with 0.1 μM magnetic nanoparticles; and (iii) T_2 = 4.09 ms for the agarose-based phantom with 3.5 μM magnetic nanoparticles. One can also see that in this case, a concentration of 3.5 μM magnetic nanoparticles is too high. For smaller echo times (*e.g.*, 6.5 ms) a realistic concentration of 0.1 μM magnetic nanoparticles in an agarose-based phantom provides significant contrast and is usable. As a side observation, internal inhomogeneity can also be seen in the prepared phantom samples (see Fig. 9).

Clinical relevance: MRI studies with a 1.5 Tesla clinical system. Fig. 10 provides a direct comparison between Gd-based contrast agents and magnetic nanoparticles in agarose-based phantoms, allowing for a detailed evaluation of their imaging performance at different concentrations. The second and third rows display similar concentrations of magnetic nanoparticles and Gadovist embedded in agarose-based phantoms, highlighting their behavior across a wide range of concentrations. The last column of every row displays a control sample, which serves as a reference to confirm that the observed signal variations are due to the presence of contrast agents.

At higher concentrations, specifically 10, 5.00, 2.50, 1.25, and 0.68 μM, the magnetic nanoparticles tend to aggregate due to their inherent magnetic dipole interactions, forming large clusters. This aggregation alters their MRI behavior, causing a transition from T1 contrast enhancement to T2-dominant effects. As these clusters grow, they create local magnetic field inhomogeneity that accelerates the dephasing of proton spins, shortening transverse relaxation times (T_2) and leading to significant signal loss. In the MRI images, this appears as dark regions instead of the expected bright contrast. However, such high concentrations are not used in clinical practice, as contrast agents are carefully optimized to remain well-dispersed. This effect is specific to magnetic nanoparticles due to their

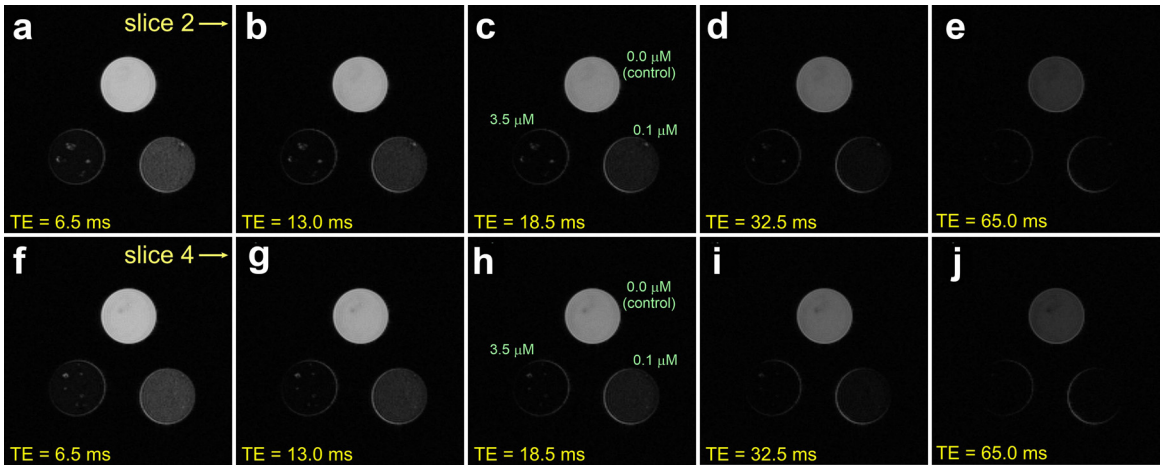

Fig. 9 MR image recorded at 11.7 T magnetic field induction for three agarose phantom samples with 0 (control), 0.1 and 3.5 μM magnetic nanoparticle concentrations, with a repetition time TR = 2.6 s and different echo times (a) and (f) TR = 0.49 s; (b) and (g) TR = 0.99 s; (c) and (h) TR = 2.99 s; (d) and (i) TR = 7.99 s and (e) and (g) TR = 9.99 s exploring the transverse relaxation time T_2.

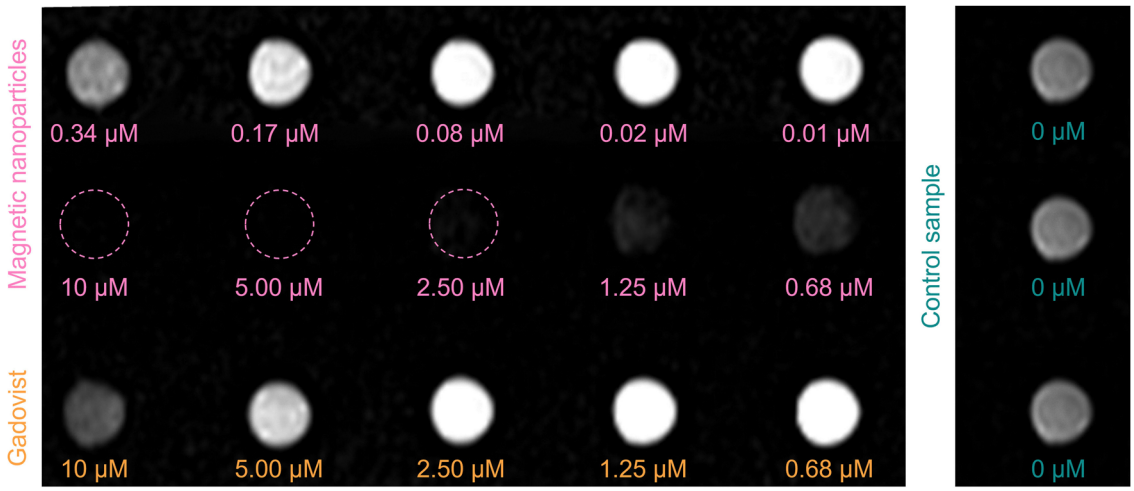

Fig. 10 Comparison of T_1-weighed signal alteration recorded at 1.5 T between magnetic nanoparticles (top and middle rows, at concentrations given as nanoparticle molarity) and Gadovist (bottom row) embedded in agarose-based phantoms at varying concentrations. The last column represents the control sample.

magnetic properties and does not occur with Gadovist. Unlike magnetic nanoparticles, Gd lacks ferromagnetic or superparamagnetic properties, preventing dipole–dipole interactions and clustering. As a result, Gd-based contrast agents remain well-dispersed in solution regardless of concentration.

At intermediate concentrations −0.17, 0.08, and 0.02 μM – magnetic nanoparticles exhibit contrast enhancement that is as effective as that achieved using Gadovist. These concentrations result in bright signals in MRI scans, demonstrating that magnetic nanoparticles can function as T1 contrast agents while maintaining good dispersion. This is significant, as it confirms that within this concentration range, magnetic nanoparticles can provide sufficient contrast enhancement for imaging applications while avoiding the long-term tissue accumulation concerns associated with Gd. Knowing these effective concentrations, future research will focus on refining and optimizing magnetic nanoparticle formulations within this range, potentially exploring slightly higher or lower concentrations to further enhance imaging performance while maintaining stability and safety.

Conventional MRI contrast agents are limited to either T1 or T2 weighted imaging modes, whereas nanoparticles with multimodal capabilities provide integrated diagnostic information. In the absence of hybrid imaging systems, using separate devices is inefficient and costly. The development of T1–T2 dual-mode contrast agents within a single nanoplatform addresses these limitations, facilitating accurate imaging of small biological targets and reducing issues related to image matching, object relocation, and discrepancies in depth penetration or resolution. T1–T2 dual-modal MRI images can be acquired by modifying pulse sequence parameters on a single MRI scanner. Building on our preclinical studies that confirmed T2-weighted signal modulation by the magnetic nanoparticles, we further evaluated their T2 imaging performance (Fig. 11).

At concentrations of 0.01, 0.02 and even 0.08 μM, the nanoparticles demonstrated measurable contrast enhancement compared to the control, suggesting their potential for dual-mode imaging. These findings indicate that our magnetic nanoparticles may contribute to improved diagnostic accuracy by providing complementary T_1 and T_2 contrast within the same imaging session. However, further investigations are necessary to optimize both the MRI acquisition parameters for T2-weighted sequences and the nanoparticles' relaxometric properties to maximize their dual-mode contrast efficiency.

Looking ahead, the prospects for this nanoparticle system are exceptionally promising. Strategic surface functionalization could address the current limitation of aggregation at high concentrations, making them highly effective MRI contrast agents across a broader range of doses. Adding an appropriate

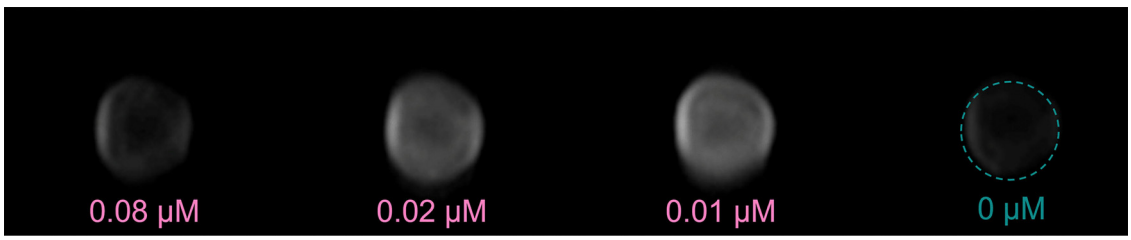

Fig. 11 Comparison of T2-weighed signal alteration recorded at 1.5 T between different concentrations of magnetic nanoparticles embedded in agarose-based phantoms and the control sample.

organic coating or other stabilizing ligands would prevent the particles from clustering when their concentration increases, preserving their MRI contrast efficiency and photothermal performance even at elevated levels. Such organic functionalization would also enhance biocompatibility, improving the nanoparticles' stability and circulation in biological environments. Moreover, it opens the door to integrating additional functionalities: the surface can be modified to attach other imaging or therapeutic agents (for multimodal imaging or combined therapies), as well as targeting ligands that direct the nanoparticles to specific tissues or tumor cells.

Nonetheless, for future translation to biological applications, aspects such as long-term biocompatibility, *in vivo* clearance, and biodistribution will require thorough evaluation. These factors are critical to ensuring safety, minimizing off-target effects, and confirming that the nanoparticles maintain performance in complex physiological environments. By systematically addressing these challenges in upcoming studies, the current system could evolve into a clinically relevant platform. These enhancements would transform our nanoparticles into a versatile platform for precision medicine – a multifunctional theranostic agent capable of targeted MRI diagnostics and effective photothermal treatment.

4. Conclusions

This comprehensive study demonstrates the dual-functionality of our magnetic nanoparticles, validating their use as both MRI contrast agents and photothermal therapeutic agents activated by NIR irradiation. With a nanoscale size of 9.23 ± 2.97 nm and strong magnetic properties ($M_s \approx 52.4$ emu g^{-1}), the nanoparticles showed robust contrast enhancement in both T1 and T2 MRI modes across clinically relevant concentration ranges.

By integrating data from both an 11.7 Tesla preclinical MRI and a 1.5 Tesla clinical scanner, we assessed the performance of these nanoparticles under realistic imaging conditions. Comparisons with the clinical agent Gadovist reveal a slightly lower contrast efficiency on a per-molecule basis, yet our system provides notable advantages in terms of safety, flexibility in dosing, and potential theranostic integration. These benefits are critical for PTT, where higher local concentrations at the tumor site are often required for therapeutic efficacy, achievable through passive or active targeting strategies.

A key innovation of this study is the use of tissue-mimicking agarose phantoms doped with optical scatterers, which simulate both the optical and thermal diffusion characteristics of real tissue. To the best of our knowledge, this is among the first systematic evaluation of Fe_3O_4 nanoparticles as sole photothermal agents under NIR irradiation in a 3D tissue-mimicking environment, bridging the gap between basic *in vitro* solution studies and *in vivo* applications. At 970 nm – the optimal wavelength in our setup – the penetration depth reached 2.1 cm, with a photothermal conversion efficiency of 71.59% and heating levels sufficient for mild hyperthermia, all achieved under medically safe irradiation power.

While this work does not include biological *in vitro* or *in vivo* validation, the multi-level phantom modeling, clinical MRI testing, and adherence to safety standards provide a strong preclinical foundation for future translational studies. The current platform is intended as a realistic, scalable evaluation model, and *in vivo* investigations are part of our next phase of development.

In summary, we present a multifunctional nanoplatform that unites imaging and therapy capabilities, validated under conditions that closely reflect clinical contexts. This approach not only supports the safe implementation of magnetic nanoparticles in MRI-guided photothermal therapy but also lays the groundwork for their eventual translation into targeted, minimally invasive cancer treatment.

Conflicts of interest

There are no conflicts of interest to declare.

Data availability

The data supporting the findings of this study are available within the article and its SI files. Additional data that support the findings of this study, including raw data and detailed experimental protocols, are available from the corresponding author upon reasonable request.

Supplementary information is available. See DOI: **https://doi.org/10.1039/d5tb01160d**.

Acknowledgements

Raluca Borlan is thankful for the 'Grant for young scientists', awarded by Babes-Bolyai University, under contract number SRG-UBB 32995/23.06.2023. Andreea Balmus is thankful for the Special Scholarship for Scientific Activity (contract number 35804/28.11.2024) funded by Babes-Bolyai University. Radu Fechete acknowledges the Ministry of Research, Innovation and Digitization, as the Intermediary Body which partially supported the work in the framework of the Operational Programme Competitiveness 2014–2020 project code SMIS 2014+ 127725, contract no. 352/390028/23.09.2021, acronym project INSPIRE; and the Ministry of European Investment and Projects (MIPE) as Managing Authority for the Smart Growth, Digitalization and Financial Instruments Programme 2021–2027 and the Ministry of Research, Innovation and Digitalization (MCID) as Intermediary Research Body, project code SMIS 2021+ 324771 contract MIPE no. G-2024-71962/23.10.2024 and contract MCID no. 390005/23.10.2024, project acronym INSPIRE-II. Sample preparation for transmission electron microscopy, image acquisition and analysis were performed at European Commission, Joint Research Centre (JRC), Ispra, Italy, in the frame of the 'Training and Capacity Building session 2024' organised by the JRC Nanobiotechnology laboratory. A preprint version of this manuscript was previously posted on Authorea (DOI: **https://www.authorea.com/users/921237/articles/1293374**).

References

1 J. F. Liu, B. Jang, D. Issadore and A. Tsourkas, Use of magnetic fields and nanoparticles to trigger drug release and improve tumor targeting, *Wiley Interdiscip. Rev.: Nanomed. Nanobiotechnol.*, 2019, **11**, e1571.
2 R. Lapusan, R. Borlan and M. Focsan, Advancing MRI with magnetic nanoparticles: a comprehensive review of translational research and clinical trials, *Nanoscale Adv.*, 2024, **6**, 2234–2259.
3 S. D. Kong, *et al.*, Magnetic targeting of nanoparticles across the intact blood–brain barrier, *J. Controlled Release*, 2012, **164**, 49–57.
4 C. F. G. C. Geraldes, Rational Design of Magnetic Nanoparticles as T1–T2 Dual-Mode MRI Contrast Agents, *Molecules*, 2024, **29**, 1352.
5 X. Xia, *et al.*, Magnetic Graphitic Nanocapsules: Fabrication, Classification, and Theranostic Applications, *Chem. Biomed. Imaging*, 2023, **1**, 683–691.
6 Z. Li, *et al.*, Designing Smart Iron Oxide Nanoparticles for MR Imaging of Tumors, *Chem. Biomed. Imaging*, 2023, **1**, 315–339.
7 E. Forte, *et al.*, Radiolabeled PET/MRI Nanoparticles for Tumor Imaging, *J. Clin. Med.*, 2019, **9**, 89.
8 A. A. Lipengolts, *et al.*, CT and MRI Imaging of Theranostic Bimodal Fe_3O_4@Au NanoParticles in Tumor Bearing Mice, *Int. J. Mol. Sci.*, 2022, **24**, 70.
9 M. M. Van Schooneveld, *et al.*, A fluorescent, paramagnetic and PEGylated gold/silica nanoparticle for MRI, CT and fluorescence imaging, *Contrast Media Mol. Imaging*, 2010, **5**, 231–236.
10 T.-H. Shin, Y. Choi, S. Kim and J. Cheon, Recent advances in magnetic nanoparticle-based multi-modal imaging, *Chem. Soc. Rev.*, 2015, **44**, 4501–4516.
11 L. Racca and V. Cauda, Remotely Activated Nanoparticles for Anticancer Therapy, *Nano-Micro Lett.*, 2021, **13**, 11.
12 Y.-F. Zhang and M. Lu, Advances in magnetic induction hyperthermia, *Front. Bioeng. Biotechnol.*, 2024, **12**, 1432189.
13 R. Borlan, M. Focsan, D. Maniu and S. Astilean, Interventional NIR Fluorescence Imaging of Cancer: Review on Next Generation of Dye-Loaded Protein-Based Nanoparticles for Real-Time Feedback During Cancer Surgery, *Int. J. Nanomedicine*, 2021, **16**, 2147–2171.
14 X. Hou, *et al.*, Multifunctional near-infrared dye-magnetic nanoparticles for bioimaging and cancer therapy, *Cancer Lett.*, 2017, **390**, 168–175.
15 R. Gupta and D. Sharma, Manganese-Doped Magnetic Nanoclusters for Hyperthermia and Photothermal Glioblastoma Therapy, *ACS Appl. Nano Mater.*, 2020, **3**, 2026–2037.
16 B. Nasseri, *et al.*, Nanomaterials for photothermal and photodynamic cancer therapy, *Appl. Phys. Rev.*, 2022, **9**, 011317.
17 S. Cabana, A. Curcio, A. Michel, C. Wilhelm and A. Abou-Hassan, Iron Oxide Mediated Photothermal Therapy in the Second Biological Window: A Comparative Study between Magnetite/Maghemite Nanospheres and Nanoflowers, *Nanomaterials*, 2020, **10**, 1548.
18 S. Wang and Y. Hou, Photothermal therapy based on magnetic nanoparticles in cancer, *J. Appl. Phys.*, 2021, **130**, 070902.
19 S. Fu, Y. Man and F. Jia, Photothermal Effect of Superparamagnetic Fe_3O_4 Nanoparticles Irradiated by Near-Infrared Laser, *J. Nanomater.*, 2020, **2020**, 1–8.
20 A. R. Trifoi, *et al.*, Coprecipitation nanoarchitectonics for the synthesis of magnetite: a review of mechanism and characterization, *React. Kinet., Mech. Catal.*, 2023, **136**, 2835–2874.
21 S. Palanisamy and Y.-M. Wang, Superparamagnetic iron oxide nanoparticulate system: synthesis, targeting, drug delivery and therapy in cancer, *Dalton Trans.*, 2019, **48**, 9490–9515.
22 I. Nkurikiyimfura, Y. Wang, B. Safari and E. Nshingabigwi, Temperature-dependent magnetic properties of magnetite nanoparticles synthesized via coprecipitation method, *J. Alloys Compd.*, 2020, **846**, 156344.
23 *Magnetic Properties of Fine Particles*, ed. J. L. Dormann and D. Fiorani, Elsevier, 1992, DOI: 10.1016/C2009-0-13025-8.
24 M. Anbarasu, M. Anandan, E. Chinnasamy, V. Gopinath and K. Balamurugan, Synthesis and characterization of polyethylene glycol (PEG) coated Fe_3O_4 nanoparticles by chemical co-precipitation method for biomedical applications, *Spectrochim. Acta, Part A*, 2015, **135**, 536–539.
25 L. F. Gomez–Caballero, *et al.*, Facile synthesis of Fe_3O_4 nanoparticles at room temperature coated with meso-2,3-dimercaptosuccinic acid for improved biocompatibility, *J. Nanopart. Res.*, 2023, **25**, 66.
26 Y. Liu, *et al.*, Effects of crystal size and sphere diameter on static magnetic and electromagnetic properties of monodisperse Fe_3O_4 microspheres, *Mater. Chem. Phys.*, 2016, **173**, 152–160.
27 D. Serantes and D. Baldomir, Nanoparticle Size Threshold for Magnetic Agglomeration and Associated Hyperthermia Performance, *Nanomaterials*, 2021, **11**, 2786.
28 B. Freis, *et al.*, Defects or no defects? Or how to design 20–25 nm spherical iron oxide nanoparticles to harness both magnetic hyperthermia and photothermia, *Nanoscale*, 2024, **16**, 20542–20555.
29 K. Bilici, A. Muti, F. Demir Duman, A. Sennaroğlu and H. Yağcı Acar, Investigation of the factors affecting the photothermal therapy potential of small iron oxide nanoparticles over the 730–840 nm spectral region, *Photochem. Photobiol. Sci.*, 2018, **17**, 1787–1793.
30 R. Han, *et al.*, Ultralow-intensity near infrared light synchronously activated collaborative chemo/photothermal/photodynamic therapy, *Biomater. Sci.*, 2020, **8**, 607–618.
31 R. J. Thomas, *et al.*, A procedure for laser hazard classification under the Z136.1-2000 American National Standard for Safe Use of Lasers, *J. Laser Appl.*, 2002, **14**, 57–66.
32 K. Kaczmarek, R. Mrówczyński, T. Hornowski, R. Bielas and A. Józefczak, The Effect of Tissue-Mimicking Phantom Compressibility on Magnetic Hyperthermia, *Nanomaterials*, 2019, **9**, 803.

33 J. A. Curcio and C. C. Petty, The Near Infrared Absorption Spectrum of Liquid Water, *J. Opt. Soc. Am.*, 1951, **41**, 302.
34 E. E. McCabe-Lankford, T. L. Brown and N. H. Levi-Polyachenko, Assessing fluorescence detection and effective photothermal therapy of near-infrared polymer nanoparticles using alginate tissue phantoms, *Lasers Surg. Med.*, 2018, **50**, 1040–1049.
35 J. Estelrich and M. A. Busquets, Iron Oxide Nanoparticles in Photothermal Therapy, *Molecules*, 2018, **23**, 1567.
36 M. E. Sadat, *et al.*, Photoluminescence and photothermal effect of Fe_3O_4 nanoparticles for medical imaging and therapy, *Appl. Phys. Lett.*, 2014, **105**, 091903.
37 X. Zhang, *et al.*, Composite Photothermal Platform of Polypyrrole-Enveloped Fe_3 O_4 Nanoparticle Self-Assembled Superstructures, *ACS Appl. Mater. Interfaces*, 2014, **6**, 14552–14561.
38 M. Kong, Y. Huang, R. Yu and J. Xi, Coordination bonding-based Fe_3O_4@PDA-Zn2 + -doxorubicin nanoparticles for tumor chemo-photothermal therapy, *J. Drug Delivery Sci. Technol.*, 2019, **51**, 185–193.
39 I. B. Yeboah, S. W. K. Hatekah, Y. K. Konku-Asase, A. Yaya and K. Kan-Dapaah, Destruction of Fibroadenomas Using Photothermal Heating of Fe_3O_4 Nanoparticles: Experiments and Models, *Appl. Sci.*, 2020, **10**, 5844.
40 M. E. Sadat, *et al.*, Effects of Nanoscale Structures on Photothermal Heating Behaviors of Surface-Modified Fe_3 O_4 Nanoparticles, *Nano LIFE*, 2019, **09**, 1950001.
41 X. Wang, *et al.*, Enhanced photothermal-photodynamic therapy for glioma based on near-infrared dye functionalized Fe_3O_4 superparticles, *Chem. Eng. J.*, 2020, **381**, 122693.
42 Y. Wang, *et al.*, Enzyme-instructed self-aggregation of Fe_3 O_4 nanoparticles for enhanced MRI T_2 imaging and photothermal therapy of tumors, *Nanoscale*, 2020, **12**, 1886–1893.
43 R. Ge, *et al.*, Fe_3 O_4 @polydopamine Composite Theranostic Superparticles Employing Preassembled Fe_3 O_4 Nanoparticles as the Core, *ACS Appl. Mater. Interfaces*, 2016, **8**, 22942–22952.
44 H. Peng, *et al.*, Highly Ligand-Directed and Size-Dependent Photothermal Properties of Magnetite Particles, *Part. Part. Syst. Charact.*, 2016, **33**, 332–340.
45 J. Guo, W. Wei, Y. Zhao and H. Dai, Iron oxide nanoparticles with photothermal performance and enhanced nanozyme activity for bacteria-infected wound therapy, *Regener. Biomater.*, 2022, **9**, rbac041.
46 J. Ling, S. Gong and Y. Xia, Monodisperse Fe_2 O_3 Suprapartricles: Eco-Friendly Fabrication, Gallic Acid Modification, Size-Dependent Photothermal Conversion Efficiency, and Cellular Uptake, *Adv. Mater. Interfaces*, 2020, **7**, 2000804.
47 J. Wang, *et al.*, MR/SPECT Imaging Guided Photothermal Therapy of Tumor-Targeting Fe@Fe_3 O_4 Nanoparticles in Vivo with Low Mononuclear Phagocyte Uptake, *ACS Appl. Mater. Interfaces*, 2016, **8**, 19872–19882.
48 B. Getiren, Z. Çıplak, C. Gökalp and N. Yıldız, NIR-responsive Fe_3 O_4 @ PPy nanocomposite for efficient potential use in photothermal therapy, *J. Appl. Polym. Sci.*, 2020, **137**, 49343.
49 H. Peng, *et al.*, Nuclear-Targeted Multifunctional Magnetic Nanoparticles for Photothermal Therapy, *Adv. Healthcare Mater.*, 2017, **6**, 1601289.
50 Y. Oh, J.-Y. Je, M. S. Moorthy, H. Seo and W. H. Cho, pH and NIR-light-responsive magnetic iron oxide nanoparticles for mitochondria-mediated apoptotic cell death induced by chemo-photothermal therapy, *Int. J. Pharm.*, 2017, **531**, 1–13.
51 S. Wang, *et al.*, Red-blood-cell-membrane-enveloped magnetic nanoclusters as a biomimetic theranostic nanoplatform for bimodal imaging-guided cancer photothermal therapy, *J. Mater. Chem. B*, 2020, **8**, 803–812.
52 T. M. T. Vo, *et al.*, Rice starch coated iron oxide nanoparticles: A theranostic probe for photoacoustic imaging-guided photothermal cancer therapy, *Int. J. Biol. Macromol.*, 2021, **183**, 55–67.
53 K. Tao, *et al.*, Targeted multifunctional nanomaterials with MRI, chemotherapy and photothermal therapy for the diagnosis and treatment of bladder cancer, *Biomater. Sci.*, 2020, **8**, 342–352.
54 G. Li, *et al.*, The construct of triple responsive nanocomposite and its antibacterial effect, *Colloids Surf., B*, 2022, **212**, 112378.
55 S. K. Shaw, *et al.*, γ-Fe_3O_4 nanoflowers as efficient magnetic hyperthermia and photothermal agent, *Appl. Surf. Sci.*, 2021, **560**, 150025.
56 C.-C. Huang, *et al.*, New insight on optical and magnetic Fe_3 O_4 nanoclusters promising for near infrared theranostic applications, *Nanoscale*, 2015, **7**, 12689–12697.
57 J. Ham, H. Kim and H. Cho, Photothermal Conversion Performance of Fe_3O_4/ATO Hybrid Nanofluid for Direct Absorption Solar Collector, *Energies*, 2024, **17**, 5059.
58 G. Gao, X. Sun and G. Liang, Nanoagent-Promoted Mild-Temperature Photothermal Therapy for Cancer Treatment, *Adv. Funct. Mater.*, 2021, **31**, 2100738.
59 R. Borlan, *et al.*, Dual-Modal Near-Infrared Organic Nanoparticles: Integrating Mild Hyperthermia Phototherapy with Fluorescence Imaging, *Int. J. Nanomedicine*, 2024, **19**, 9071–9090.
60 P. Vaupel, *et al.*, From Localized Mild Hyperthermia to Improved Tumor Oxygenation: Physiological Mechanisms Critically Involved in Oncologic Thermo-Radio-Immunotherapy, *Cancers*, 2023, **15**, 1394.
61 S. D. Oberdick, *et al.*, Iron oxide nanoparticles as positive T1 contrast agents for low-field magnetic resonance imaging at 64 mT, *Sci. Rep.*, 2023, **13**, 11520.

